Noise Robust Image Edge Detection based upon the Automatic Anisotropic Gaussian Kernels

WeiChuan Zhang[1,2], YaLi Zhao[1], Toby P. Breckon[2], Long Chen[3]

[1]Xi'an Polytechnic University, Xi'an, 710048, China
[2] Durham University, UK
[3] Bournemouth University, UK
E-mail: zwc2003@163.com, weichuan.zhang@durham.ac.uk

Abstract: This paper presents a novel noise robust edge detector based upon the automatic anisotropic Gaussian kernels (ANGKs), which also addresses the current problem that the seminal Canny edge detector may miss some obvious crossing edge details. Firstly, automatic ANGKs are designed according to the noise suppression, edge resolution and localization precision, which also conciliate the conflict between them. Secondly, reasons why cross-edge points are missing from Canny detector results using isotropic Gaussian kernel are analyzed. Thirdly, the automatic ANGKs are used to smooth image and a revised edge extraction method is used to extract edges. Finally, the aggregate test receiver-operating-characteristic (ROC) curves and Pratt's Figure of Merit (FOM) are used to evaluate the proposed detector against state-of-the-art edge detectors. The experiment results show that the proposed algorithm can obtain better performance for noise-free and noisy images.

Key Words: automatic anisotropic Gaussian kernels, anisotropic directional derivatives (ANDDs), edge detection, Canny detector.

1. Introduction

Edge detection is a fundamental operation in computer vision and image processing. It concerns detecting significant variations in gray level images. The outputs of edge detectors, namely edge maps, are the foundation of high-level image processing, such as object tracking [1], image segmentation [2] and corner detection [3]. Various methods have been developed, including the differentiation-based methods [4-7], statistical methods [8, 9], machine learning methods [10, 11], active contour method [12], multiscale methods [13-19], and the anisotropic diffusion or selective smoothing methods [20-24].

In gray level images, edges may be defined as sharp changes in intensity and most common types include steps, lines, and junctions. Differentiation of intensity is a direct characterization of sharp

changes. Early Robert, Sobel, and Prewitt operators used different derivative filters for edge detection [4]. Differentiation of an image is an ill-posed problem that noise and texture probably incur spurious edge. To regularize the differentiation, images are smoothed by a low-pass kernel before differentiation. In the pioneering work of Canny [5], the optimal kernels are derived to be isotropic Gaussian kernels with a scale parameter (the standard deviation of Gaussian function), in terms of the Canny's theory: insensibility to noise, good edge localization, and unique response to one edge. The Canny detector widely used up to now cascades Gaussian smoothing, gradient calculation, non-maxima suppression, and bi-threshold decision. By contrast, the Marr-Hildreth detector [14] cascades Gaussian smoothing, Laplacian operator, and zero-crossing detection. In these two notable detectors and their modified version [9], an isotropic Gaussian kernel with a predefined scale incurs the duality between edge detection and localization precision. An isotropic Gaussian kernel with a large scale achieves good detection capability but the blurred edges degrade localization precision and resolution [6]. It is just reverse for a Gaussian kernel with a small scale. To amend the duality "detection versus localization", ones developed the multiscale edge detection and the edge enhancement via anisotropic diffusion or selective smoothing.

Edges in images exhibit multiscale characteristics. The contours of small structures are suitable to be detected in fine scales while the boundaries of larger objects are suitable to be detected in coarse scales. In [15], it was proved that a multiscale Canny edge detection is equivalent to finding the local maxima of a wavelet transform. The edge map is extracted from the wavelet modulus maxima of an image. Moreover, the image itself can be also approximately restored from these wavelet modulus maxima. In a similar vien, various multiscale transforms are applied to analyze images and to capture edge information. The typical examples include contourlets [16], ridgelets [18], and shearlets [16]. In [16][17], two efficient multiscale and multi-directional detectors via the shearlet transform were developed.

Alternatively, the Gaussian smoothing of images may equivalently be viewed as the solution of the heat conduction or diffusion equation [21]. Various anisotropic diffusion or selective smoothing methods based upon PDE were developed for image denoising, edge detection, and segmentation [22-24]. The anisotropic diffusion based upon partial differential equation (PDE) provides an iterative and adaptive Gaussian smoothing of images, where the kernels are matched to the micro-local structures around each pixel in scales and directions. The anisotropic diffusion based upon PDE

realizes edge region focusing before detection and the followed Canny-type operator performs edge extraction from smoothed images [24]. It is noticed that iterative and adaptive smoothing algorithms are computationally expensive and the corresponding edge detectors are not fast in implementation.

Lampert and Wirjadi [25] analyzed the reason that isotropic Gaussian are so popular is that isotropic Gaussian filter has only one parameter, which makes it easy to handle analytically, and simple to implement. However, from the image processing perspective, ANGKs are more interesting, because a set of ANGKs [3][6][26] can characterize anisotropic local structures (such as edges and corners) accurately. In [27], a fast anisotropic Gaussian filtering algorithm based upon the convolution filters or recursive filters was developed, where an anisotropic 2D Gaussian filter is decomposed into a 1D Gaussian filter in the x-direction followed by a 1D filter in a non-orthogonal direction. However, it still has no prior work explicitly concerns itself with the design of anisotropic and scale factor of ANGKs for edge detection.

In this paper, the automatic anisotropic factor of ANGKs is designed under the principles of high signal-to-noise ratio (SNR), fine localization, and high edge resolution. Subsequently, the reasons why some edge points are missing from the Canny edge detectors are analyzed. A revised edge tracking method is presented, which overcome some limitations of the Canny edge detector based upon the isotropic Gaussian kernel. Finally, a novel noise robust edge detection algorithm is proposed. Compared with four state-of-the-art edge detectors [5][6][9][19] based upon the aggregate test receiver operating characteristic (ROC) curves and the Pratt's Figure of Merit (FOM), the experimental results show that the proposed detector can obtain better performance for noise-free and noisy images.

This paper is organized as follows. In section 2, characteristics of the AGNKS and ANDDs are introduced, and the automatic scales selection of ANGKs for edge detection is presented. A revised edge tracking method and a novel edge detection algorithm are presented in section 3. The new edge detector is compared with the four state-of-the-art detectors, and performance analysis is described in section 4. Finally, we conclude our paper in section 5.

2. Anisotropic Gaussian Kernels and Directional Derivative Vector

It is indicated [14] that the conflict between the edge localization precision and noise-sensitivity is reconcilable for a single isotropic Gaussian kernel. In this section, we first introduce the properties of the ANGKs and ANDDS; and then, a set of automatic anisotropic Gaussian kernels are designed to

conciliate this conflict.

2.1 Anisotropic Gaussian kernels and directional derivatives filters

In the spatial domain, the ANGKs can be represented [3][6] as follows

$$
g_{\sigma,\rho,\theta}(\mathbf{x}) = \frac{1}{2\pi\sigma^2} \exp\left(-\frac{1}{2\sigma^2} \mathbf{x}^T \mathbf{R}_{-\theta} \begin{bmatrix} \rho^2 & 0 \\ 0 & \rho^{-2} \end{bmatrix} \mathbf{R}_{\theta} \mathbf{x} \right),
$$
$$
\mathbf{R}_{\theta} = \begin{bmatrix} \cos\theta & \sin\theta \\ -\sin\theta & \cos\theta \end{bmatrix},
$$

(1)

where $\mathbf{x}=[x,y]^T$, σ is the scale factor ($\sigma > 0$), ρ is the anisotropic factor ($\rho \geq 1$) and $\mathbf{R}_{\theta}$ is the

rotating matrix. When a noisy image corrupted by zero-mean white noise $w(\mathbf{x})$ with a variance σ_w^2 is

smoothed by an anisotropic Gaussian kernel in (1), noise suppression can be evaluated by the noise

variance in the smoothed image:

$$
\begin{aligned}
\sigma_{\bar{w}}^2 &= E\left\{ \left(w * g_{\sigma,\rho,\theta}(\mathbf{x}) \right)^2 \right\} \\
&= \iint \iint g_{\sigma,\rho,\theta}(\mathbf{u}) g_{\sigma,\rho,\theta}(\bar{\mathbf{u}}) E\{w(\mathbf{x}-\mathbf{u})w(x-\bar{\mathbf{u}})\} d\mathbf{u} d\bar{\mathbf{u}} \\
&= \sigma_w^2 \iint \iint g_{\sigma,\rho,\theta}(\mathbf{u}) g_{\sigma,\rho,\theta}(\bar{\mathbf{u}}) \delta(\mathbf{u}-\bar{\mathbf{u}}) d\mathbf{u} d\bar{\mathbf{u}} \\
&= \sigma_w^2 \iint \left(g_{\sigma,\rho,\theta}(\mathbf{u}) \right)^2 d\mathbf{u} = \frac{\sigma_w^2}{4\pi\sigma^2}
\end{aligned}
$$

(2)

where $\sigma_{\bar{w}}^2$ denote the variance of the smoothed noise. Equation (2) shows that the noise suppression

capability of an ANGK depends on only its scale but it is independent of its anisotropic factor and

direction.

For an anisotropic Gaussian kernel $g_{\sigma,\rho,\theta}(\mathbf{x})$, an anisotropic directional derivative (ANDD) filter is

derived as follows:

$$
\varphi_{\sigma,\rho,\theta}(\mathbf{x}) = \frac{\partial g_{\sigma,\rho}}{\partial x}\left(\mathbf{R}_{\theta}\mathbf{x} \right) = -\frac{[\cos\theta, \sin\theta]\mathbf{x}}{\sigma^2 \rho^{-2}} g_{\sigma,\rho,\theta}(\mathbf{x}).
$$

(3)

The anisotropic directional derivative of an input image $I(\mathbf{x})$ along the direction θ is computed

by the convolution operator

$$
\nabla_{\sigma,\rho} I(\mathbf{x},\theta) = I * \varphi_{\sigma,\rho,\theta}(\mathbf{x}).
$$

(4)

An ANGK with $\sigma^2 = 6, \rho^2 = 6, \theta = \pi / 4$, and its corresponding ANDD filter are shown in Fig. 1.
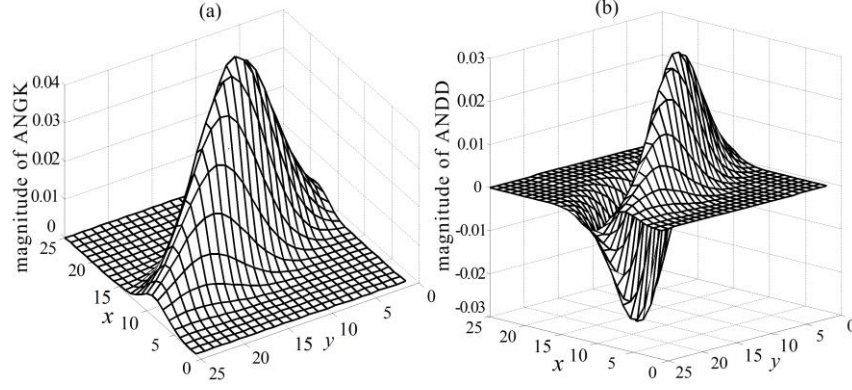
Fig.1 An ANGK (a) and its corresponding ANDD filter (b) with $\sigma^2 = \rho^2 = 6$ and $\theta = \pi / 4$.

A step edge function (SEF) along direction $\vartheta + \pi/2$ is modeled as

$$SEF(\mathbf{x}) = T \cdot H([\cos \vartheta, \sin \vartheta]\mathbf{x})$$
$$H(x) = \begin{cases} 1, & x \geq 0 \\ 0, & x < 0 \end{cases}, \tag{5}$$

where T is the intensity of the gray region, $H(x)$ is the Heaviside function. The ANDD representation of the SEF is

$$\Gamma_{T,\vartheta}(\theta) = \iint_{\square^2} SEF(x, y)\varphi_{\sigma,\rho,\theta}(0 - x, 0 - y)dxdy$$
$$= \frac{T \cos(\theta - \vartheta)}{\sqrt{2\pi}\sigma\sqrt{\left(\rho^{-2}\cos^2(\theta - \vartheta) + \rho^2 \sin^2(\theta - \vartheta)\right)}}. \tag{6}$$

Equation (6) shows two important facts. Firstly, when $\theta = \vartheta$, the ANDDs achieve the maximal magnitude $T\rho/(\sqrt{2\pi}\sigma)$, which corresponds to the edge gradient. Second, the maximal value of the ANDDs at the edge is inversely proportional to the scale σ, implying smoothing images in edge detection exhibits a duality of weakening edge response whilst suppressing noise; edge gradient is directly proportional to the anisotropic factor ρ.

When $\rho = 1$, the ANGKs degenerate into a single isotropic Gaussian kernel. The previous analysis in equation (2) shows that the noise suppression capability of the ANGKs only depend on the scale. Thus, in the same scale, using ANGKs instead of isotropic Gaussian kernel increase the signal-to-noise ratio (SNR) of the edge responses and improve edge detection performance. In Fig.2, we plot the magnitude of the anisotropic directional derivatives of the step edge with $\vartheta = \pi / 4, T = 1$ in two scales $\sigma = 1$ and 2 and two anisotropic factors $\rho = 1$ (isotropic) and $\rho = 6$ (anisotropic). Obviously, with increasing of scale, the edges are blurred heavier and the

maximal magnitude of the directional derivatives at the edge is reduced. When anisotropic kernels are used, the smoothing along the edge direction blurs less edges and the maximal magnitude of the directional derivatives at the edge preserves a larger value, which is helpful to detect weak step edges in noisy images.
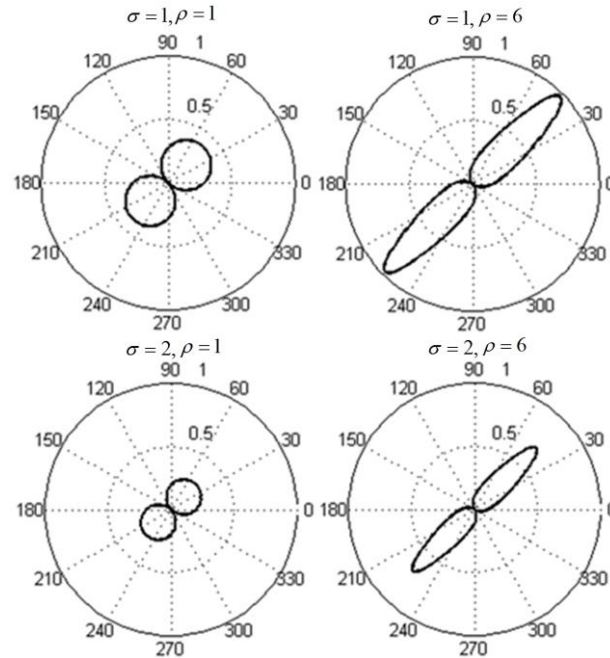

Fig.2 Magnitudes of the anisotropic directional derivatives at a unit-strength step edge along $45°$ for scales $\sigma = \{1, 2\}$ and anisotropic factors $\rho = \{1, 6\}$.

In [26], we also have proved that the directional derivative response of the ANGKs have the ability to characterize the properties of the local structure accurately. A step edge, simple L edge, a Y-type edge, an X-type edge, and a star-like edge are shown in the first row of Fig. 3, where T_i is the intensity of each wedge-shape region. The corresponding ANDDs are demonstrated in the second row of Fig. 3. As comparison, the last row of Fig.3 illustrates the directional derivative response of the isotropic Gaussian with $\sigma=\rho =1$ for five type edge points. It can be seen that the isotropic Gaussian is unable to discriminate the structure information of edge pixels, which may affect the accuracy of edge detection, especially in the cross-edges. This is one of the reasons why Canny edge detector miss some cross-edges, which will be illustrated in Section 3.1 in detail.
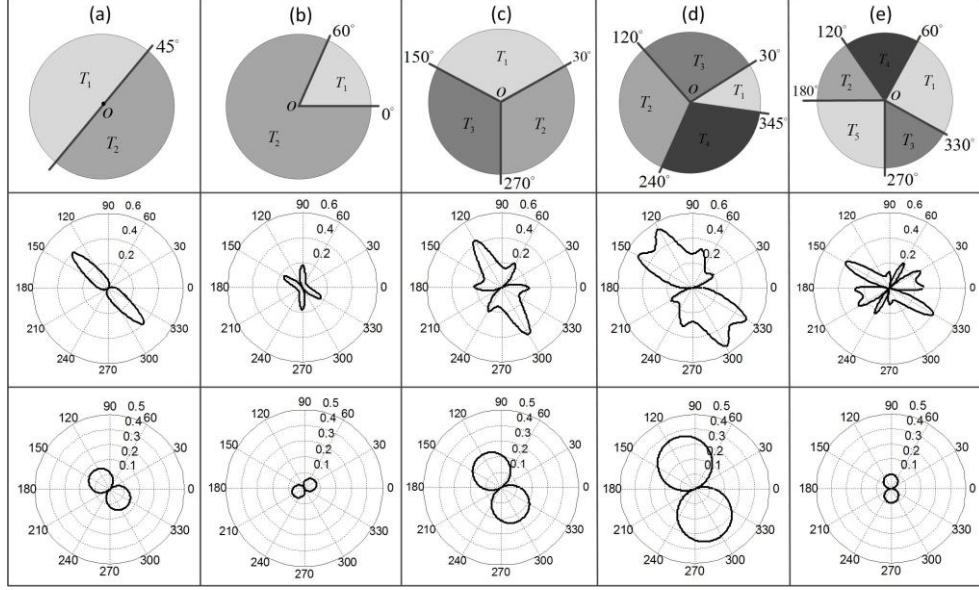
Fig.3 A step edge, a L-type edge, a Y-type edge, an X-type edge, and a star-like edge are plotted in (a)-(e) at the first row, the corresponding ANDDs are plotted in the second row, and the corresponding isotropic directional derivatives are plotted in the third row for comparison.

2.2 Automatic anisotropic factor for edge detection

The input image is the discrete signal in the integer lattice $\square^2$. Under this way, the continuous ANGKs and ANDD filters must be discretized. For given scale, anisotropic factor and oriented angles $\theta_k = (k-1)\pi / K$, $k = 1, 2, \cdots, K$, sampling the ANGKs in (1) and ANDD filters in (3), the discrete ANGKs and ANDD filters are obtained as follows:

$$g_{\sigma,\rho,k}(\mathbf{n}) = \frac{1}{2\pi\sigma^2} \exp\left(-\frac{1}{2\sigma^2} \mathbf{n}^T \mathbf{R}_k^T \begin{bmatrix} \rho^2 & 0 \\ 0 & \rho^{-2} \end{bmatrix} \mathbf{R}_k \mathbf{n} \right),$$

$$\varphi_{\sigma,\rho,k}(\mathbf{n}) = -\frac{[\cos\theta_k, \sin\theta_k]\mathbf{n}}{\sigma^2 \rho^{-2}} g_{\sigma,\rho,k}(\mathbf{n}) \tag{7}$$

$$\mathbf{R}_k = \begin{bmatrix} \cos\theta_k & \sin\theta_k \\ -\sin\theta_k & \cos\theta_k \end{bmatrix}, \mathbf{n} = \begin{bmatrix} n_x \\ n_y \end{bmatrix} \in \square^2.$$

Below consider the automatic anisotropic factor for edge detection. Canny [5] suggested that the optimal edge detector should maximize both signal-to-noise ratio (SNR) and localization. In terms of (2) and (6), for a step edge with the direction $\vartheta + \pi/2$ and a direction derivative filter $\varphi_{\sigma,\rho,k}$, the SNR of the edge response is

$$SNR(\sigma, \rho, \theta, \vartheta) \equiv \frac{1}{\sigma_{\bar{w}}} \left| \Gamma_{T,\beta}(\theta) \right| = \frac{\sqrt{2}T \left| \cos(\theta - \vartheta) \right|}{\sigma_w \sqrt{\left(\rho^2 \sin^2(\theta - \vartheta) + \rho^{-2} \cos^2(\theta - \vartheta) \right)}}. \tag{8}$$

It can be seen that the SNR of the edge response depend upon noise level, the difference between

the edge direction and smoothed direction, and the anisotropic factor while is independent of the scale. Moreover, it also reveals an important fact: when a fixed Gaussian kernel is used to detect isolate step edge, the detection probability is independent of the scale of the kernel at a given false alarm probability, because the reduction of the edge response and noise level resulted from the smoothing are direct proportional. We use

$$SNR(\sigma, \rho, K) = \min_{\vartheta \in [0,\pi]} \max_{k=1,2,\cdots,K} \left\{ SNR(\sigma, \rho, \theta_k, \vartheta), \theta_k = (k-1)\pi / K \right\}$$
$$= \frac{\sqrt{2}T \left| \cos\left(\frac{\pi}{2K}\right) \right|}{\sigma_w \sqrt{\left(\rho^2 \sin^2\left(\frac{\pi}{2K}\right) + \rho^{-2} \cos^2\left(\frac{\pi}{2K}\right) \right)}}$$

(9)

to evaluate the insensibility to noise of the set of anisotropic Gaussian kernels. Meanwhile, we have proved [6] that the edge resolution and localization precision of the ANGKs are proportional to the resolution constant $\zeta(\sigma, \rho, K)$

$$\zeta(\sigma, \rho, K) \equiv \max_{\vartheta \in [0,\pi]} \min_{k=1,2,\cdots,K} \left\{ \zeta(\sigma, \rho, \theta_k, \beta) \right\}$$
$$= 2\sigma \sqrt{\left(\rho^2 \sin^2\left(\frac{\pi}{2K}\right) + \rho^{-2} \cos^2\left(\frac{\pi}{2K}\right) \right)} .$$

(10)

The smaller it is, the higher the edge resolution and localization precision of the ANGK is. In terms of Canny criteria in edge detection [5], for a given the scale σ and the number K of the kernels, the optimal anisotropic factor is required to maximize $SNR(\sigma, \rho, K)$ to achieve the insensibility to noise whilst to minimize $\zeta(\sigma, \rho, K)$ to achieve high edge resolution and localization precision. Here, the automatic anisotropic factor for edge detection is selected by maximizing the ratio $SNR(\sigma, \rho, K)$ and $\zeta(\sigma, \rho, K)$ for given scale σ and the number K of the kernels. It can be obtained by

$$\rho_{aut}(K) = \arg\max_{\rho} \left\{ \frac{SNR(\sigma, \rho, K)}{\zeta(\sigma, \rho, K)} \right\}$$
$$= \arg\max_{\rho} \left\{ \frac{T \left| \cos\left(\frac{\pi}{2K}\right) \right|}{\sqrt{2}\sigma\sigma_w \left(\rho^2 \sin^2\left(\frac{\pi}{2K}\right) + \rho^{-2} \cos^2\left(\frac{\pi}{2K}\right) \right)} \right\} = \frac{1}{\sqrt{\tan\left(\frac{\pi}{2K}\right)}}$$

(11)

From equation (11), when only two directional derivative filters are used, $\rho_{aut} = 1$ corresponds to the isotropic Gaussian kernel and its two partial derivative filters in the traditional Canny detector. When $K = 8$, $\rho_{aut} = 1/\sqrt{\tan(\pi/16)} \approx 2.2422$. To obtain enough information of gray variation, the default of the orientation number is set to 8. Meanwhile, the capability of ANDD filters to suppress noise [6] is inversely proportional to the square of the scale and the square of the ratio to

the scale to the anisotropic factor. Under this way, we always take $\sigma \geq \rho$ in applications to assure that the sampled kernels and derivative filters inherit more features of their continuous versions.

An example of the isotropic Gaussian-based edge strength map (ESM) and the automatic ANDD-based ESM is shown in Fig. 4. The test image with Gaussian standard deviation $\varepsilon_w = 15$ is shown in Fig. 4 (a). The isotropic Gaussian based ESM is shown in Fig. 4(b), which suffers from edge blurring effect and 'dirty' background resulted from the noise. The reason is that isotropic Gaussian kernel does not have the ability to suppress noise and obtain high edge resolution. The ANDD-based ESM is shown in Fig. 4 (c), which has high edge resolution and clear background. The reason is that the designed automatic ANGKs have considered the edge localization, resolution and noise-robustness.

$$I = \frac{R+G+B}{3} \tag{1}$$

$$H = \cos^{-1}\left\{ \frac{\frac{1}{2}[(R-G)+(R-B)]}{\sqrt{(R-G)^2+(R-B)(G-B)}} \right\} \tag{2}$$

$$S = 1 - \frac{3\min(R,G,B)}{R+G+B} \tag{3}$$

(a) a noisy image with $\varepsilon_w = 15$

(b) ESM of the Isotropic Gaussian based
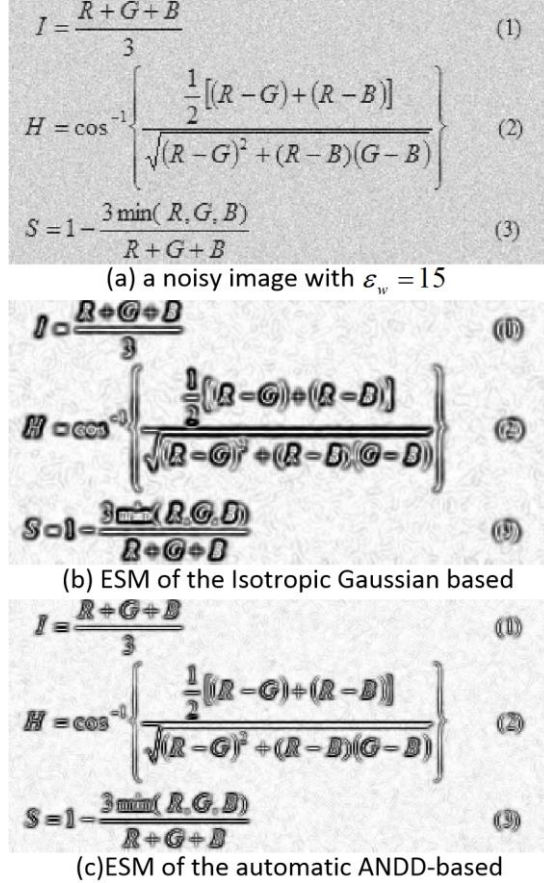

(c)ESM of the automatic ANDD-based

Fig.4 Illustration of the ESMs of a noisy image: (a) a noisy image with $\varepsilon_w = 15$; (b) ESM of the isotropic Gaussian based; (c) ESM of the automatic ANDD-based.

3. Edge Detection using Automatic ANGKs

In this section, we first introduce the Canny detector deficiencies. It follows that a new revised edge extraction is given, which depend upon gradient vector in an image and non-maxima

suppression method. Finally, a novel edge detection algorithm using automatic ANGKs is presented.

3.1 The problem of Canny algorithm

In Canny algorithm, an edge pixel is defined as if the gradient magnitude at either side of it is less than the gradient at the pixel. Based upon the definition, the operation of non-maxima suppression is used to extract edges, which may cause crossing edge points missing detection. For step edge pixel, the gradient direction is always normal to step edge, which is easily extracted under the edge definition of Canny; however, the gradient direction of other type edge points (such as Y-type edge, X-type edge, and star-like edge) are influenced by the gray value of each wedge-shape component, as the second row of the Fig.3 shown. Under the Canny definition, the crossing edge points may be missing detection. This phenomenon also occurs around the crossing edge points.
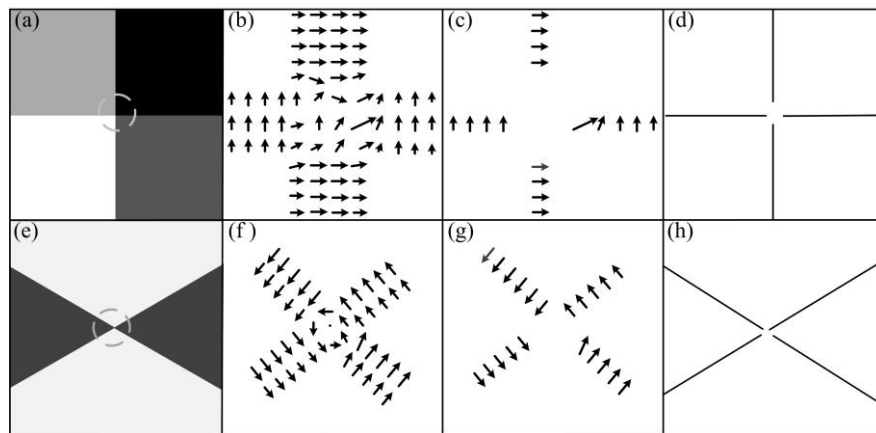

Fig.5Edge detection by Canny detector. (a) and (e) show two different experiment images, respectively. (b) and (f) illustrate the gradient vectors of image (a) and (e), respectively. (c) and (g) illustrate the gradient vectors after non-maximum suppression of image (a) and (e), respectively. (d) and (h) illustrate the edges of (a) and (e) detected by the Canny detector, respectively.

Two examples are demonstrated in Fig. 5. Two images with four well-defined homogenous region and symmetrical gray region are shown Fig .5 (a) and (e), respectively. The two images center exist crossing edges (marked by '∘'). The gradient vectors of the crossing edge regions using Canny detector are shown in Fig. 5 (b) and (f), respectively. The length and direction of arrows indicate the gradient magnitude and direction, respectively. Fig. 5(b) shows that the gradient magnitudes of the image center of Fig. 5(a) are larger than those of pixels adjacent to them. However, the gradient direction of the contour may not be normal to the contour. Fig. 5(f)

shows that the gradient magnitude of the image center pixel of the Fig. 5(e) is zero (proof is very simple, omitted here), and its surrounding pixels gradients are small. After non-maximum suppression, some true edges of the two image center regions are suppressed, as shown in Fig. 5 (c) and (g), respectively. The results of the Canny detector are shown in Fig. 5 (e) and (h), respectively. We see that edges near the image center are missed.

3.2 A revised edge detection algorithm using ANGKs

To overcome the edge missing problem of Canny edge detector, a revised edge tracking method using automatic ANGKs is proposed in this subsection.

For an input image $x(\mathbf{n})$, the anisotropic directional derivatives are calculated by

$$y_k(\mathbf{n}) = x(\mathbf{n}) * \varphi_{\sigma,\rho,k}(\mathbf{n}) = \sum_{\boldsymbol{\tau}} \varphi_{\sigma,\rho,k}(\boldsymbol{\tau}) x(\mathbf{n} - \boldsymbol{\tau}) . \tag{12}$$

The obtained K images contain edge information along K directions, and then the edge strength map (ESM) of the image in terms of the discrete forms is derived by

$$\mathrm{ESM}x(\mathbf{n}) = \max_{k=1,2,\cdots,K} \left\{ |y_k(\mathbf{n})| \right\} , \tag{13}$$

which is equal with the gradient magnitude at each pixel in an image. Moreover, the edge gradient direction map (EGDM) of the image can be extracted by

$$\mathrm{EGDM}x(\mathbf{n}) = \left(\arg\max_k \left\{ |y_k(\mathbf{n})| \right\} \right) \times \frac{\pi}{K} . \tag{14}$$

After ESM and EGDM are obtained by ANGKs, non-maximum suppression and hysteresis thresholds technique by Canny algorithm [5] are applied to select candidate edge pixels. If gradient magnitude of a pixel is larger than two neighbors in the gradient direction, the pixel is marked as candidate edge pixel. Subsequently, if the pixel stronger than the upper threshold (T_h) is marked as strong candidate edge; otherwise, the edge pixel between the two thresholds is marked as weak candidate edge. The rest of pixels are marked as the background. As a result, the revised edge tracking follows the steps below.

1. Edge tracking based upon the strong and weak candidate edges set is implemented by BLOB-analysis (Binary Large OBject). The ESM is scanned from left to right, top to bottom. The first strong candidate edge pixel is declared an edge. It follows that all its neighbors are recursively followed till no other candidate edge pixels connect to it, and those weak candidate edges are marked as edges if they have been connected to strong

edges. Furthermore, each edge contour is marked with a unique label. Under this way, the initial edge map Ω is obtained $\Omega = \{E_1, E_2, \cdots, E_m\}$, E_i $(i = 1, 2, \cdots, m)$ represents the $i'th$ edge contour.

2. Determining the structure for each edge contour. For the $s'th$ edge contour $E_s = \{P_1, P_2, \cdots, P_n\}$, $P_j = (x_j, y_j)$ ($j = 1, 2, \cdots, n$) is the position of the $j'th$ pixel on the edge contour. Let d be the distance between the initial point P_1 and final point P_n on the $s'th$ edge contour, and if $d \leq D_{\max}$, then E_s is labeled as a loop edge contour; otherwise, E_s is labeled as an open edge contour. Here, $D_{\max}$ is defined as the maximum admissible distance between P_1 and P_n, we set $D_{\max} = 4$.

3. Supposing that E_s is a loop contour and $P_1 \neq P_n$, the gap between the initial and final points will be filled by the shortest distance between them.

4. If E_s is an open contour, the endpoint P_1 or P_n contains an endpoint Q_n of another contour in a specified size (5×5), fill the gap between the two endpoints by the shortest distance and connect the two edge contour into an open contour. Otherwise, the endpoint P_1 or P_n contains edge pixels of another edge contour, then the gradient direction of the endpoint and its neighborhood pixels are considered; calculating the mean gradient direction of the endpoint and its neighboring pixels (for $D_{\max} = 4$), and then the endpoints is extended to another edge contour along the direction perpendicular to the mean gradient direction. Repeat the procedure till the each endpoint of the neighborhood does not contain other endpoints.

Fig. 6 shows a full procedure from edge detection to edge contour extraction and extension. Fig. 6(a) is the test image. The magnified image of part (a) (marked by '▢') is shown in Fig. 6(b), which is used to demonstrate the edge extraction and extension. Fig. 6(c) shows the edge detection result by the proposed method. Fig. 6(d) plots the edge contour extracted from the edge map. Fig .6(e) illustrates the result of the contours after filling small gaps and edge extension. It can be seen that most of the missed cross-edges in the edge detection are picked up by the filling gaps and edge extension; for instance, the broken contours "41" and "42" are removed into a loop contour, the contours "58", "59" and "61" are connected into a long contour. The final detection result of the test image (a) is shown in Fig. 6(f).
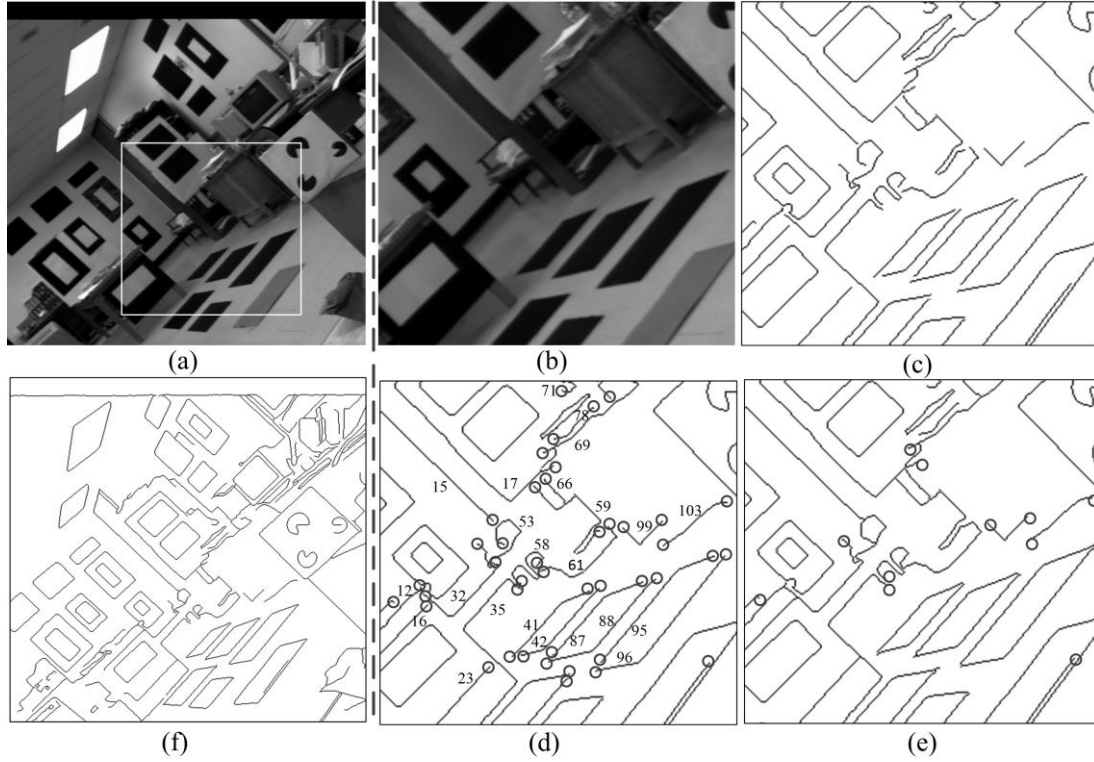
Fig.6 Demonstration of edge extraction and extension (a) test image, (b) magnitude image of the part (a), (c) the result of edge detection by the proposed method, (d) the edge contour extracted from the edge map, (e) the results of fill gaps and edge extension, (f)the final detection result of the test image.

3.3 Edge Detection Algorithm via Automatic ANGKs

The proposed method first smooth the input image by ANGKs and obtain the ANDDs of each pixel. It follows that the ESM and EGDM are derived as the edge measure. The outline of the proposed algorithm is:

1. The input image is smoothed by the automatic ANGKs.

2. Calculate the ANDDs of the input image in terms of equation (12).

3. Calculate the edge strength map $ESMx(\mathbf{n})$ and the edge gradient direction map $EGDMx(\mathbf{n})$ from the ANDDs in terms of equations (13) and (14).

4. For each pixel, gradient magnitude and direction are used to the non-maximum suppression. If gradient magnitude at either side of it is less than the gradient at the pixel in the gradient direction, retain the pixel; otherwise, it would be set to zero.

5. Hysteresis thresholds are used to select the candidate edge pixels, and the revised edge tracking method is used to edge extraction.

4. Experimental Results and Performance Evaluation

In this section, we focus on experiments and performance evaluation. The proposed detector is compared with four detectors, Canny [5], the statistical [9], the IAGKs [6] and the multi-scale Sobel [19] in terms of the empirical receiver operating characteristic (ROC) curves [28] and Pratt's Figure of Merit (FOM) [29].

4.1 Empirical ROC evaluation

Bowyer et al. [28] proposed a statistical analysis method using ROC curves to evaluate different edge detectors, which use real images, manually specified ground truth (GT), adaptive sampling parameter space and train-and-test evaluation. Its kernel is to compare the results of detectors under individual optimal parameter settings. For a test image with the GT that contains N_e edge pixels and N_{ne} non-edge pixels, an edge pixel is detected by the detector within a specified tolerance of an edge in the GT, then it is counted as a true positive (TP); otherwise, an edge pixel is detected in a no-edge region, it is counted as a false positive (FP). Additionally, edge pixels are detected in a don't-care region do not account as TPs or FPs. Subsequently, if a detector at a given parameter setting detects N_{TP} correct edge pixels and N_{FP} false edge pixels; then the ROC curve of a detector at the specified parameter setting is obtained by the points (%Unmatched GT Edges, %FP Edges), which are defined by

$$\%Unmatched\ GT\ Edges \equiv 1 - \frac{N_{TP}}{N_e}, \quad \%FP\ Edges \equiv \frac{N_{FP}}{N_{ne}}. \tag{15}$$

In this format of the ROC curve, the ideal point is (0, 0) and an ROC curve which lies to the lower left of another curve is better. The aggregate ROC curves were introduced in [28] for performance evaluation, where a detector parameter setting are first trained to attain the best ROC curve on a single image and then tested on the set of images to obtain the aggregate test ROC curve by averaging the aggregate ROC curves of all the images. The image database for training and testing, coming from the image datasets [28], contains a set of fifty object images and another set of ten aerial images with the specified GT.

The Canny [5] detector has three adjustable parameters, the Gaussian-smoothing scale σ, the percent of not-edge pixels ς, and the factor of threshold ratio τ. In the ROC curve computation, the parameter settings are taken in the set

$$\begin{cases} \sigma = 1, 1.2, ..., 5 \\ \varsigma = 0.6, 0.61, ..., 0.95 \\ \tau = 0.2, 0.21, ..., 0.6 \end{cases}. \tag{16}$$

The statistical [9] method has three adjustable parameters, the Gaussian-smoothing scale σ, the percent of not-edge pixels ς, and the factor of threshold ratio τ. In the ROC curve computation, the parameter settings are taken in the set

$$\left\{ \begin{array}{l} \sigma = 1,1.2,...,5 \\ \varsigma = 0.6, 0.61,...,0.95 \\ \tau = 0.2, 0.21,...,0.6 \end{array} \right\}. \tag{17}$$

The IAGKs [6] method has four adjustable parameters, the anisotropic factor ρ and scale factor σ, the percent of not-edge pixels ς, and the factor of threshold ratio τ. The parameter settings are taken in the set

$$\left\{ \begin{array}{l} \sigma^2 = 2,3,...,12 \\ \rho^2 = 2,3,...,12 \\ \varsigma = 0.6, 0.61,...,0.95 \\ \tau = 0.2, 0.21,...,0.6 \end{array} \right\}. \tag{18}$$

The multi-scale Sobel [19] has three adjustable parameters, the difference between two consecutive scales $\Delta\sigma$, the setting of multi-scale Gaussian smoothing S, the maximal displacement of an edge in two consecutive scales T_{dist}. The parameter settings are taken in the set

$$\left\{ \begin{array}{l} \Delta\sigma = 0.1, 0.25, 0.5 \\ S = \{0.5\}, \{0.5, 0.5 + \Delta\sigma\},..., \\ \qquad \{0.5, 0.5 + \Delta\sigma,..., 6\} \\ T_{dist} = 1, 2, 3 \end{array} \right\}. \tag{19}$$

The proposed method has five adjustable parameters, the number of orientations K, the anisotropic factor $\rho = 1 / \sqrt{\tan\left(\frac{\pi}{2K}\right)}$, scale factor σ, the percent of not-edge pixels ς, and the factor of threshold ratio τ. The parameter settings are taken in the set

$$\left\{ \begin{array}{l} K = 4, 6,...., 16 \\ \sigma^2 = \rho^2, \rho^2 + 1,..., \rho^2 + 10 \\ \varsigma = 0.6, 0.61,..., 0.95 \\ \tau = 0.2, 0.21,..., 0.6 \end{array} \right\}. \tag{20}$$
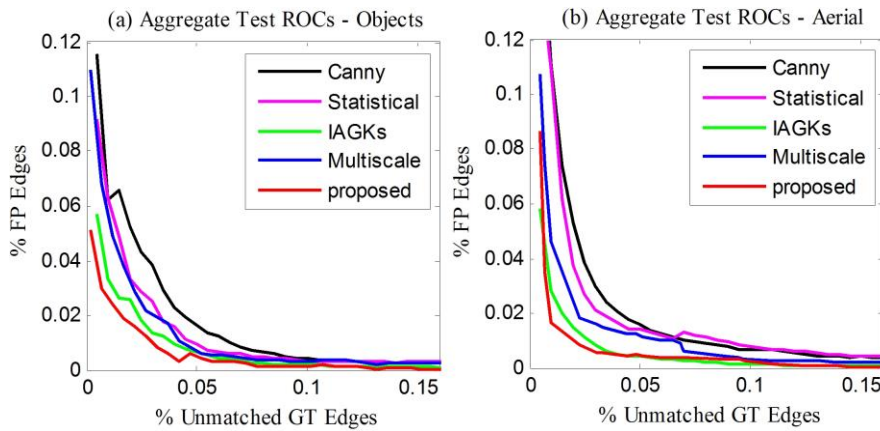

Fig.7 Comparison of the aggregate test ROC curves of the five detectors for the set of object images and aerial images. (a) Aggregate test ROC curves-Objects. (b) Aggregate test ROC curves-Aerials.

The results shown in Fig. 7 are the ROC curves at the noise-free case. The proposed detector

offers the best performance among the five detectors. The IAGKs [6] attains the second best. The major reason is that statistical, Canny and Multi-scale Sobel detectors use the isotropic Gaussian to smooth the input image and the derivatives of x- and y-axis are used to extract the image gray-variation and structure information; however, the edge is the anisotropic feature, isotropic Gaussian kernel cannot represent the image's gray-variation information well. On the contrary, the automatic ANGKs can extract the fine image gray-variation information, which is helpful to detect weak edges. This is the major reason that the proposed method and IAGKs detector achieve the greater performance improvement on the aerial images than three other detectors. Furthermore, a revised edge extraction is presented to overcome the limitations of the existing differential-based methods, which cause some obvious edge pixels missing.
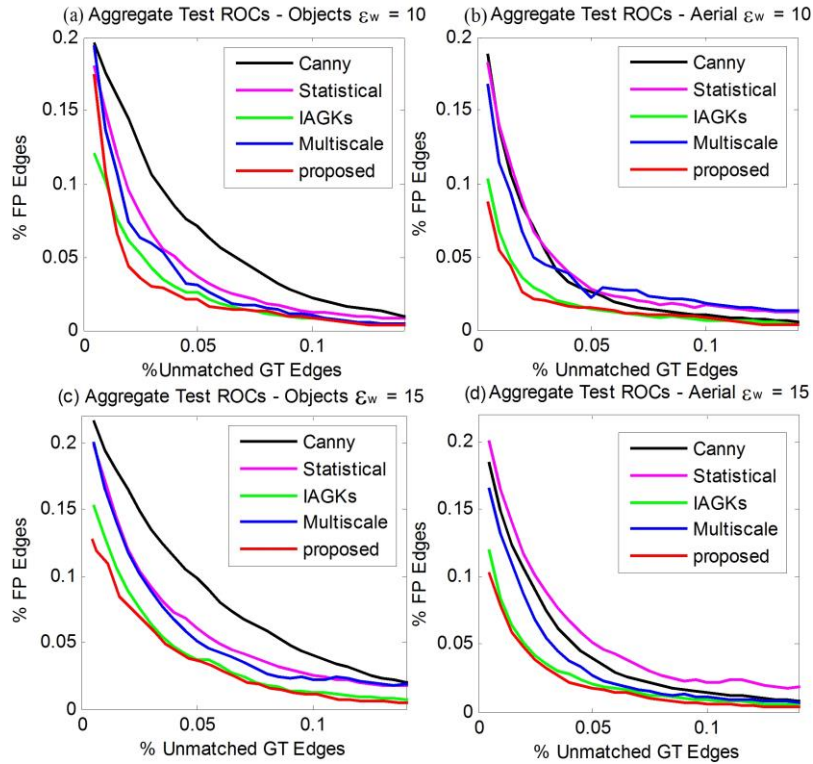

Fig.8 Comparison of the aggregate test ROC curves of the five detectors for the set of object images and aerial images. (a) Aggregate test ROC curves-Objects $\varepsilon_w = 10$. (b) Aggregate test ROC curves-Aerials $\varepsilon_w = 10$. (c) Aggregate test ROC curves-Objects $\varepsilon_w = 15$. (d) Aggregate test ROC curves-Aerials $\varepsilon_w = 15$.

The noise-robustness of an edge detector is important in applications, because images are inevitably corrupted by noise in acquisition and transmission. Here, zero-mean white Gaussian noise of standard deviation 10 and 15 are added to test images to verify the noise-robustness, respectively. Fig .8 demonstrates the ROC curves of the five detectors for the noise cases. As the noise standard variation increases, the performance of the five detectors decreases in different degrees. Meanwhile, the results represent that the proposed method achieves the best noise-robustness than the other four detectors. This is owing to the fact that the automatic ANGKs have the ability to extract the fine gray-variation and noise

suppression. The revised edge extraction can greatly reduce the occurrence probability of cross-edges missing. Meanwhile, we have noticed that the difference in the performance of the proposed method and IAGKs method [6] is not obvious. The reason is that the test samples are limited，the phenomenon is more prominent on the 10 aerial test images. Meanwhile, the parameter settings of the ANGKs in IAGKS method [6] play the biggest advantage in the rule of ROC evaluation.

Furthermore, the BSDS500 image datasets [2] are used to further evaluate the five detectors. Compared with the image datasets [28], the manually specified GTs of the BSDS500 image datasets also include edge pixels and non-edge pixels, while do not have don't care edge region. We used 50 images for training and algorithm development. The 200 test images were used to generate the final results for this paper. The results shown in Fig. 9 are the ROC curves at the noise-free and noisy cases. In the noise-free case, the proposed achieves the highest performance. The IAGKs [6] attains the second best. The other three edge detectors performed substantially poorer. The main reason is that the isotropic Gaussian kernel has not the ability to extract gray intensity variation information well. In the noisy case, the performance of the proposed detector provides more significant improvements, owing to its noise-robustness and good edge connectivity. The IAGKs [6] obtains the second best for the ANGKs are robust to the noise. The other three detectors substantially lack noise robustness, because noise suppression of the isotropic Gaussian kernel is at the cost of edge localization loss.
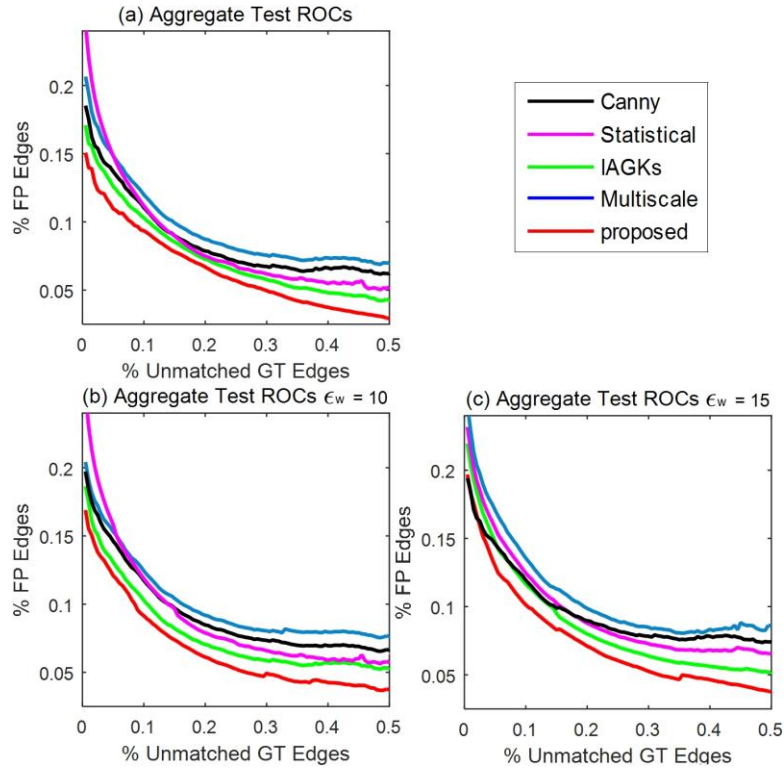

Fig.9 Comparison of the aggregate test ROC curves of the five detectors for the set of BSD500 test images. (a) Aggregate test ROC curves. (b) Aggregate test ROC curves $\varepsilon_w = 10$. (c) Aggregate test ROC curves $\varepsilon_w = 15$.

4.2 FOM evaluation

Pratt's Figure of Merit (FOM) [29] is another popular performance evaluation tool, which does not require ground truth images. FOM measures the deviation of a detected edge point from the ideal edge. It is defined as

$$FOM = \frac{1}{\max\{N_d, N_i\}} \sum_{k=1}^{N_d} \frac{1}{1+\lambda d^2(k)}, \tag{21}$$

where N_i is the number of the edge points on the ideal edge, N_d is the number of detected edge points, $d(k)$ is the distance between the k-th detected edge pixel and the ideal edge, λ is scaling constant (here $\lambda = 1/4$). In all cases, FOM ranges from 0 to 1, where 1 corresponds to a perfect match between the detected edge map and the ideal edge map.

Fig.10.Ten test images for the FOM evaluation

In this experiment, ten test images with different scenes, as shown in Fig.10, collected from the literature on edge detection, are used for FOM computation. The proposed detector (K=8, $\rho^2 = 1/\tan\left(\frac{\pi}{2K}\right)$, $\sigma^2 = 2\rho^2$), Canny [5] and IAGKs [6] use the default parameter values except for the percent of not-edge pixels and factor of threshold ratio. For each test image, its corresponding ideal edge map is attained by the Canny [5], the IAGKs [6] detectors and the proposed method in two steps. Firstly, three edge maps are obtained by the three detectors; the three edge maps have almost same number of edge pixels by tuning the percent of non-edge pixels and fixing the factor of threshold ratio at 0.5. Then, the ideal edge map is formed by the edge pixels, which exists at least two out of three edge maps. Secondly, the noise-robustness of the three detectors is evaluated by their FOM's change with noise levels based upon the ideal edge map. The percent of not-edge pixels of the three detectors is uniformly sampled from 0.6 to 0.9 with an interval 0.002 and the largest FOM of the obtained edge maps is specified as the FOM of the detector at the noise level.

Take 'Lena' image as an example, the three edge maps are shown in Fig. 11 (b)-(d); they are highly similar except for a very few details, which has 17838, 17885 and 17874 edge pixels, respectively. The ideal edge map has 17758 edge pixels, as shown in Fig. 12 (a). It is worth to note that the edge map by the proposed detector has better edge connectivity in noise free case. The main reason is that the revised edge connection method reduces the probability of the cross-edge missing.
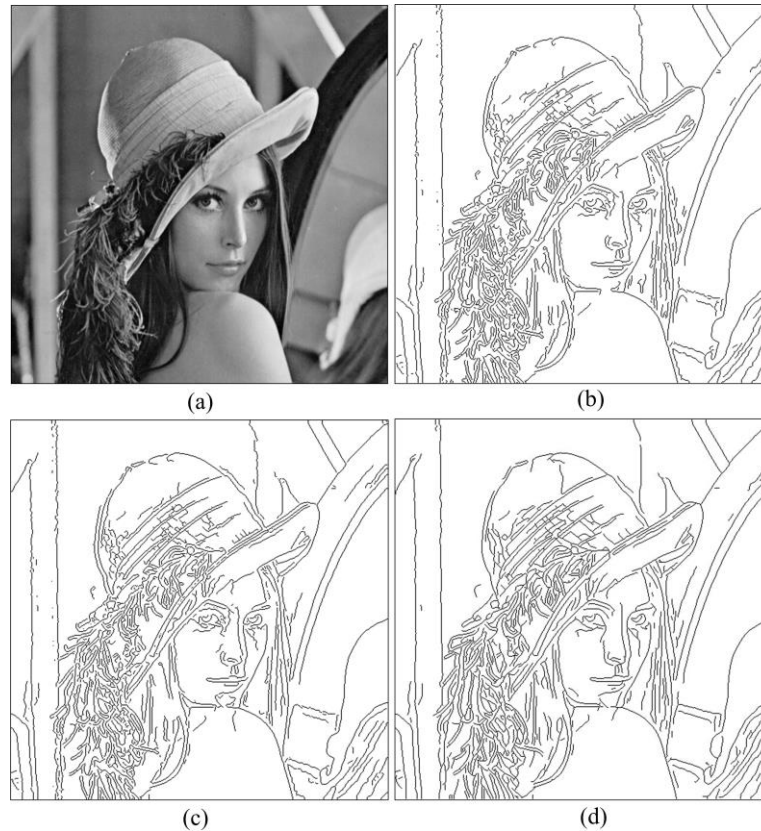

Fig.11. Edge maps by the three detectors for the noise-free 'Lena' image: (a) noise-free 'Lena' image; (b) edge map by Canny detector with the percent of non-edge pixels 0.7, (c) edge map by the IAGKs detector with the percent of non-edge pixels 0.742, and (d) edge map by the proposed detector with the percent of non-edge pixels 0.62.

At noise levels $\varepsilon_w = 5$, 10 and 15, the FOM of the three detectors are summarized in Table 1. It is easily conclude that the proposed detector achieve the best noise robustness than the two other detectors in this evaluation. The IAGKs [7] is moderate, the Canny is the poorest. The reason is that the proposed detector uses the automatic ANGKs to detect edges, which conciliates the conflict between the edge localization and noise-sensitivity. While the IAGKs detector [7] uses the experience to select the scale and anisotropic factor. The Canny detector using a single isotropic Gaussian kernel cannot conciliate this conflict [14]. As shown in Fig. 12 (b)-(d), the proposed detector attains the best edge map at $\varepsilon_w = 15$, incurs the least spurious edges. The IAGKs [7] detects a few spurious edges in smooth region and many false edges near the real edges. The Canny detector incurs quite a few

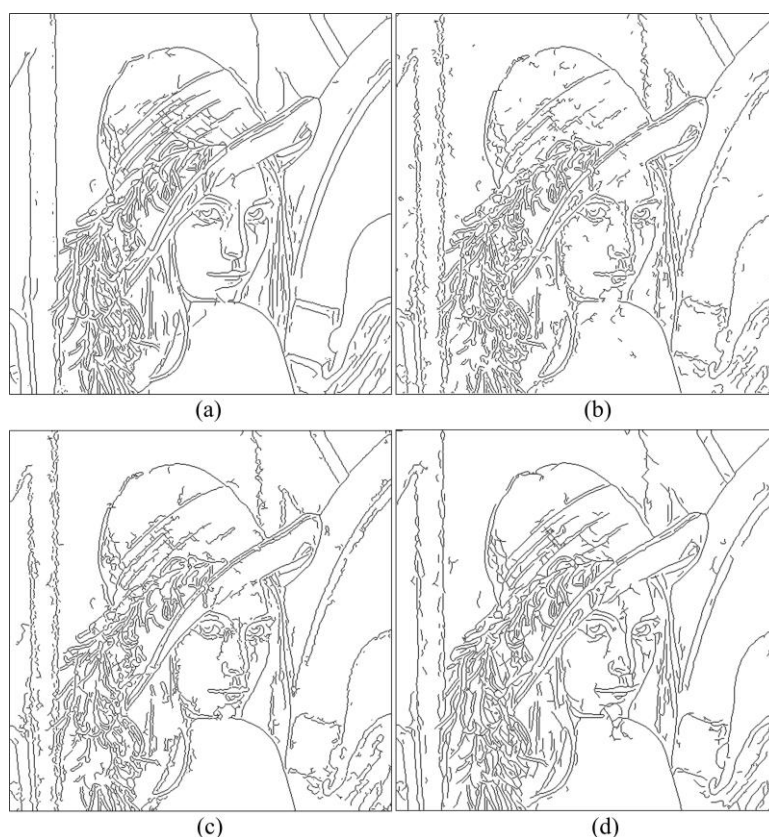false edges near the real edges and smooth region.

Fig.12. Visual comparison of the three detectors at $\varepsilon_w = 15$: (a) the ideal edge map; (b) edge map by Canny detector; (c) edge map by IAGKs detector; (d) edge map by the proposed detector.

Table I. FOM comparison of the three detectors at three noise levels,
where each cell lists FOM and the number of detected edge pixels(NDEPs).

Image name/ideal edge pixels		Canny			IAGKs[6]			Proposed		
		Noise level								
		$\varepsilon_w = 5$	$\varepsilon_w = 10$	$\varepsilon_w = 15$	$\varepsilon_w = 5$	$\varepsilon_w = 10$	$\varepsilon_w = 15$	$\varepsilon_w = 5$	$\varepsilon_w = 10$	$\varepsilon_w = 15$
Lena/17758	FOM	0.8839	0.8489	0.7992	0.8856	0.8592	0.8076	0.9247	0.8706	0.8361
	NDEPs	18039	17946	17964	18051	17770	17844	18091	17946	17920
Shave/6277	FOM	0.8318	0.7722	0.7381	0.8536	0.8054	0.7647	0.8709	0.8178	0.7885
	NDEPs	6225	6208	6210	6214	6207	6238	6287	6216	6261
Radio/15262	FOM	0.8912	0.8790	0.8543	0.9139	0.9070	0.8952	0.9339	0.9414	0.9133
	NDEPs	15283	15271	15210	15288	15308	15224	15272	15281	15271
Parking meter/13486	FOM	0.8924	0.8885	0.8872	0.9168	0.9044	0.8965	0.9241	0.9077	0.8978
	NDEPs	13526	13564	13450	13497	13552	13446	13451	13484	13494
Motorbike/13808	FOM	0.8896	0.8778	0.8662	0.9032	0.8949	0.8799	0.9282	0.9099	0.8972
	NDEPs	13762	13742	13857	13832	13741	13770	13758	13784	13806
Block/1973	FOM	0.9468	0.9360	0.9337	0.9623	0.9554	0.9413	0.9734	0.9602	0.9545
	NDEPs	1970	1988	1972	1964	1965	1968	1967	1962	1960
House/2996	FOM	0.9388	0.9300	0.9151	0.9422	0.9339	0.9205	0.9653	0.9538	0.9364
	NDEPs	2998	2992	2976	2989	2977	3010	2980	2990	3008

Peppers/10003	FOM	0.8725	0.8467	0.8314	0.8934	0.8880	0.8629	0.9023	0.8969	0.8817
	NDEPs	9971	10018	10004	10028	9986	10024	10021	10005	9997
Appreciation/9423	FOM	0.8793	0.8598	0.8393	0.9011	0.8793	0.8546	0.9175	0.8942	0.8775
	NDEPs	9424	9474	9441	9472	9425	9440	9429	9422	9390
Sofa/15139	FOM	0.8612	0.8427	0.8176	0.8955	0.8649	0.8258	0.9098	0.8869	0.8508
	NDEPs	15191	15157	15158	15146	15123	15112	15115	15191	15100

4.3 Computation complexity

The proposed edge detector has been implemented in Matlab. Detection is done on a 1.6-GHz with 4GB of memory. For each test image, the proposed algorithm was executed 100 times and mean execution times were measured. The computation complexity of the proposed algorithm is depicted in Table 2. According to Table 2, the 'Block' and 'House' image required the similar time; the 'Lena', 'Radio' and 'Parking meter' image required the more time. Note that the time slightly vary depending upon the number of detected edge pixels in the image. In the three subcomponents of the proposed detector, select candidate edge pixels consumes much more time than image smooth and revised edge tracking. Since the image fine gray variation information are derived from the eight direction ANGKs, which burden the computation complexity of the subsequent processing. Seeing that computation complexity, the proposed method should be ported to an embedded processor or FPGA controller to improve the real time performance.

Table II. Mean run-time of the proposed edge detector

Task	Time(s)				
	Block (256×256)	House (256×256)	Radio (488×611)	Parking meter (558×495)	Lena (512×512)
Image smoothing	0.169	0.171	0.486	0.416	0.4314
Select candidate edge pixels	1.425	1.432	5.114	4.577	4.901
Revised edge tracking	0.393	0.422	1.696	1.466	1.742

5. Conclusions

The main contribution of the paper is the consideration of the extraction of fine gray-variation information and the edge missing problem in the edge detection. The automatic ANGKs are designed to smooth the input image and suppress the noise; the revised edge extraction method is used to obtain the closed edge contours, which can enhance the detection accuracy and alleviate the false or missing detection. The experiment

results show that the proposed detector outperforms the four state-of-the-art edge detectors in terms of the aggregate ROC curves and Pratt's FOM evaluations.

Acknowledgments

REFERECES

[1] Pushe Zhao, Hongbo Zhu, and Tadashi Shibata, A directional-edge-based real-time object tracking system employing multiple candidate-location generation, *IEEE Trans. Image Processing*, 23(3):503-518, 2013.

[2] Pablo Arbeláez, Michael Maire, Charless Fowlkes, and Jitendra Malik, Contour Detection and Hierarchical Image Segmentation, *IEEE Trans. Pattern Anal. Mach. Intell.*, 33(5): 898-916, 2011.

[3] Wei-Chuan Zhang, Peng-Lang Shui, Contour-based corner detection via angle difference of principal directions of anisotropic Gaussian directional derivatives, *Pattern Recognition*, 48(9):2785-2797, 2015.

[4] J. Prewitt, object enhancement and extraction, *Picture process. Phychopict.,* pp.75-149, 1970.

[5] John Canny, A computational approach to edge detection, *IEEE Trans. Pattern Anal. Mach. Intell.*, 8(6): 679-698, 1986.

[6] Peng-Lang Shui, Wei-Chuan Zhang, Noise-robust edge detector combining isotropic and anisotropic Gaussian kernels, *Pattern Recognition*, 45(2): 806-820, 2012.

[7] C. Lopez-Molina, G. Vidal-Diez de Ulzurrun, J.M. Bateens, J.Van den Bulcke, B. De Bates, Unsupervised ridge detection using second order anisotropic Gaussian kernels, *Signal Processing*, 116:55-67, 2015.

[8] S. Konishi, A.L. Yuille, J.M. Coughlan, S.-C. Zhu, Statistical edge detection: learning and evaluating edge cues, *IEEE Trans. Pattern Anal. Mach. Intell.*, 25(1):57-74, 2003.

[9] Rishi R. Rakesh, Probal Chaudhuri, C. A. Murthy, Thresholding in edge detection：a statistical approach, *IEEE Trans. Image Processing*, 13(7):927-936, 2004.

[10] Shaobai Li, Srinandan D. and Koushik M., Dynamical System Approach for Edge detection using Coupled FitzHugh-Nagumo Neurons, *IEEE Trans. Image Processing*, 24(12):5206-5220, 2015.

[11] P Dollár, CL Zitnick, Fast edge detection using structured forests, *IEEE Trans. Pattern Anal. Mach. Intell.*, 37(8):1558-1570, 2015.

[12] M. Kass, A. Witkin, D. Terzopoulos, Snakes: active contour models, *International Journal of Computer Vision*, 1(4):321-331, 1987.

[13] D. Marr and E. Hildreth, Theory of edge detection. *Proc. Royal Society of London, B*, 207, pp. 187–217, 1980.

[14] S. Mallat and W-L Hwang, Singularity detection and processing with wavelets, *IEEE Trans. Inform. Theory*, 38(2): 617-643, 1992.

[15] D. D. Po and M. N. Do, Directional multiscale modeling of images using the contourlet transform, *IEEE Trans. Image Processing*, 15(6): 1610-1620, 2006.

[16] S. Yi, D. Labate, G. R. Easley, and H. Krim, A shearlet approach to edge analysis and detection, *IEEE Trans. Image Processing*, 18(5): 929-941, 2009.

[17] Miguel A. Duval-Poo, Francesca Odone, Emesto De Vito, Edge and corner with shearlets, *IEEE Trans. Image Processing*, 24(11): 3768-3781, 2015.

[18] I. W. Selesnick, R. G. Baraniuk, and N. G. Kingsbury, The dual-tree complex wavelet transform. *IEEE Signal Processing Magazine*, 22(6): 123-151, 2005.

[19] C. Lopez-Molina, B. De Bates, H. Bustince, J. Sanz, E. Barrenechea, Multi-scale edge detection based on Gaussian smoothing and edge tracking, *Knowledge-Based Systems*, 44(3):101-111, 2013.

[20] C. Lopez-Molina, M. Galar, H.Bustince, B. De Bates, On the impact of anisotropic diffusion on edge detection, *Pattern Recognition*, 47: 270-281, 2014.

[21] P. Perona and J. Malik, Scale-space and edge detection using anisotropic diffusion, *IEEE Trans. Pattern Anal. Mach. Intell.*, 12(7): 629-639, 1990.

[22] L. Alvarez, P-L Lions, J-M Morel, Image selective smoothing and edge detection by nonlinear diffusion, II, *SIAM Jour. of Numerical Analysis*, 29(3): 845-866, 1992.

[23] Song Gao and T. D. Bui, Image segmentation and selective smoothing by using Moumford-Shah Model, *IEEE Trans. Image Processing*, 14(10): 1537-1549, 2005.

[24] E. A. S. Galvanin, G. M. do Vale, and A. P. Dal Poz, The Canny detector with edge focusing using an anisotropic diffusion process, *Pattern Recognition and image analysis*, 16(4): 614-621, 2006.

[25] C. H. Lampert, O. Wirjadi, An optimal non-orthogonal separation of the anisotropic Gaussian convolution filter, *Fraunhofer ITWM*, 2005.

[26] Peng-Lang Shui, Wei-Chuan Zhang, Corner Detection and Classification using Anisotropic Directional Derivative Representations, *IEEE Trans. Image Processing*, 22(8): 3204-3219, 2013.

[27] J-M Geusebroek, A. W. M. Smeulder and J. van de Weijer, Fast anisotropic Gauss filtering, *IEEE Trans. Image Processing*, 12(8): 938-943, 2003.

[28] K. Bowyer, C. Kranenburg, A. Dougherty, Edge detector evaluation using empirical ROC curves, *Comput. Vis. Image Understand.* 84 (1):77–103, 2001.

[29] W.K. Pratt, Digital Image Processing, Wiley Interscience Publications, 1978.